Geometrical reorganization of a methane cation upon a sudden ionization: An isotope effect in electronic non equilibrium quantum dynamics

Cayo G. M. Gonçalves,[1] R. D. Levine,[2] F. Remacle[1,2,]*

[1]Theoretical Physical Chemistry, University of Liège, 4000 Liège, Belgium :
[2]The Fritz Haber Research Center for Molecular Dynamics, The Hebrew University of Jerusalem, 91904 Jerusalem, Israel

* Corresponding Author : fremacle@uliege.be

ABSTRACT

An ultrafast structural, Jahn-Teller (JT) driven, electronic coherence mediated quantum dynamics in the CH_4^+ and CD_4^+ cations that follows a sudden ionization by an XUV attopulse, exhibits a strong isotope effect. The JT effect makes the methane cation unstable in the T_d geometry of the neutral. Upon the sudden ionization the cation is produced in a coherent superposition of three electronic states that are strongly coupled. On the ground state of the cation the few femtosecond structural rearrangement leads first to a geometrically less distorted D_{2d} minimum followed by a reorganization to a shallow C_{2v} minimum. The dynamics is computed for an ensemble of 8000 ions randomly oriented with respect to the polarization of the XUV pulse. The ratio, about 3, of the CD_4^+ and CH_4^+ autocorrelation functions, is in agreement with experimental measurements of the high harmonic spectra. The high value of the ratio is attributed to the faster electronic coherence dynamics in CH_4^+.

.

KEYWORDS Ensemble averaged quantum dynamics, photoionization, non adiabatic coupling, non equilibrium electron dynamics, dynamic Jahn-Teller structural reorganization

Introduction

The Jahn-Teller (JT) effect causes the methane cation ground state (GS) to be unstable in the T_d geometry that corresponds to the equilibrium geometry of the neutral molecule. A sudden ionization of the neutral methane molecule is therefore immediately followed by a structural rearrangement of the cation. The sudden ionization leads to a superposition of the three electronic states that are degenerate at the T_d geometry. The ultrafast, few femtosecond (fs) non adiabatic dynamics triggered by the JT effect restructures the non equilibrium electronic density thereby making the structural nuclear rearrangement a test case for the role of electronic coherences in attochemistry. The first 2-3 fs of the rearrangement have been experimentally probed by high harmonic generation (HHG) spectroscopy[1, 2]. A strong isotopic effect on the CD_4/CH_4 harmonic spectra has been reported, CD_4 leading to a higher yield in emitted harmonics than CH_4 by about a factor 3 after 1.6 fs. [1, 2] The proposed explanation was that because of the slower motion of the nuclei, the time autocorrelation function, $|C(t)|^2$, falls more slowly for CD_4^+ than for CH_4^+ at the time when the electron recollides with the cation.[3] In addition, the isotope effect in CD_4/CH_4 was found to be larger than in D_2/H_2 which is not simply consistent with the changes in reduced mass.

We report here a computational study on the early, few fs, time structural quantum dynamics in CH_4^+ and CD_4^+ upon sudden ionization by an XUV attopulse. Our aim is to determine the sequence of primary changes and the reason for the large ratio of the autocorrelation functions of CD_4^+ and CH_4^+. The Franck Condon (FC) region is centered on the T_d geometry of the ground state of the neutral which is unstable in the cation. The equilibrium geometry of the ground state cation corresponds to a very shallow C_{2v} minimum that is quasi degenerate with a D_{2d} minimum. [4, 5, 6, 7] Is the less distorted D_{2d} configuration populated before the C_{2v} minimum in the very early time dynamics? This is physically reasonable since only the HCH angles need to be significantly modified during the T_d to D_{2d} rearrangement which requires a smaller

structural distortion. What is the role of the non equilibrium dynamics and of the JT non adiabatic coupling (NAC) in the large isotope effect on the high harmonic yields as measured experimentally [1, 2]? Is there indeed clear evidence for a role of non equilibrium electronic density in the very early times?

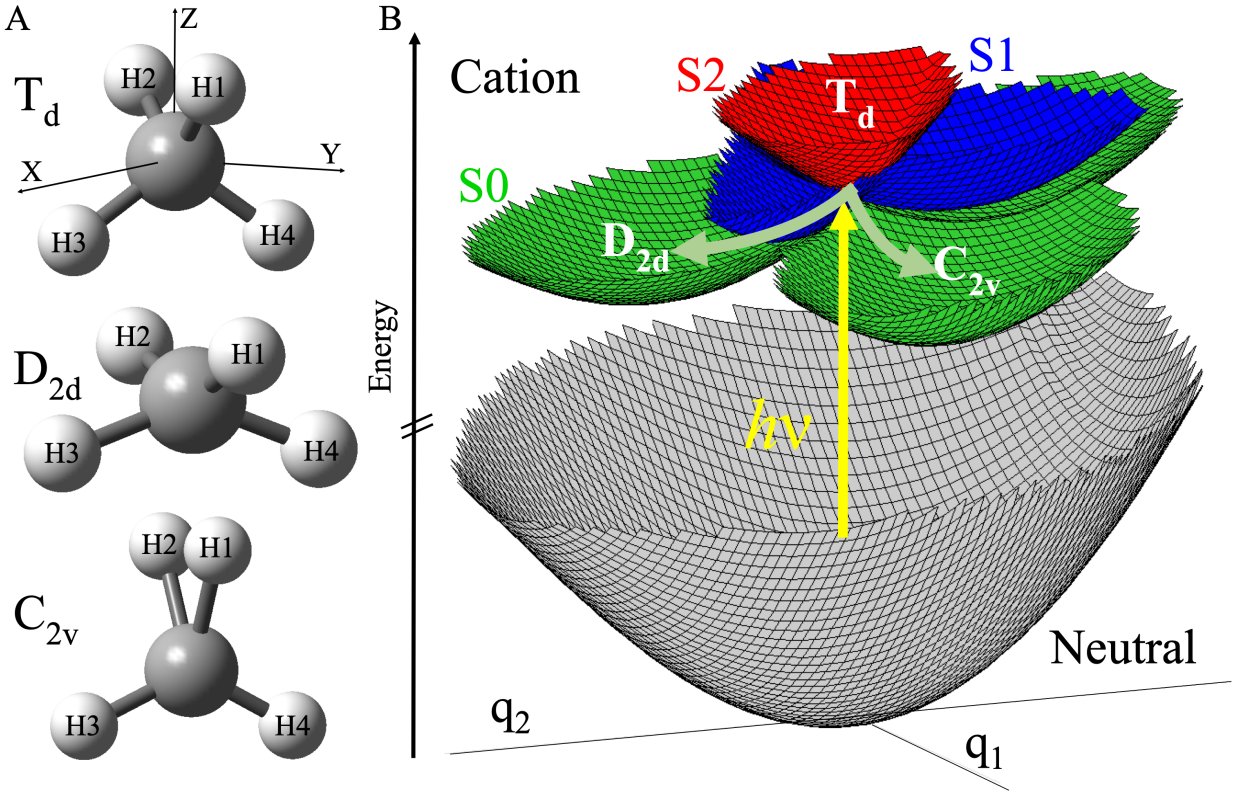

Figure 1: A. Geometries of the GS of the cation : T_d geometry and the orientation of the laboratory frame, D_{2d} and C_{2v} equilibrium geometries. B. A 3D plot of the 2-dimensional PES of the three lowest electronic states of the cation : Green : GS; blue first excited state, S1; red second excited state, S2, together with the GS of the neutral (grey). The plot is vs. two reduced coordinates: q_1, pointing to the C_{2v} minimum and q_2 pointing to the D_{2d} minimum of the GS cation respectively.

In the passage to the D_{2d} geometry the four C-H bond lengths essentially remain equal and only the valence HCH angles change with respect to the T_d geometry of the neutral while in the C_{2v} geometry, both angles and bond lengths are substantially modified, see figure 1A. The

C_{2v} and D_{2d} geometries are in the vicinity of the FC region that is defined by the ground vibrational state of the neutral at its equilibrium geometry, as shown in Figure 1B.

Patchkovskii [8] related the large isotope effect observed in the high harmonic yields of the methane cation compared to that of D_2/H_2 and its effect on the decay of the autocorrelation function, $|C(t)|^2$, to the steepness and the change of curvature of the potential energy surfaces (PES) around the JT unstable geometry. The structural rearrangement of early time JT dynamics in CH_4^+ and CD_4^+ has been studied using a quasivibronic coupling scheme[9] for the 3 lowest excited states by Mondal and Varandas up to full 9 nuclear dimensions [5, 6, 7] within the Condon approximation, assuming photoionization matrix elements independent of the nuclear geometry and neglecting the dependence of the ionization yields on the orientation of the electric field. These computations allow identifying the key role of the e and t_2 vibrational normal modes of the T_d geometry involved in the distortion leading to the C_{2v} minimum as well as the role of the t_2 mode involved in the distortion leading to the D_{2d} minimum. They confirm the ultrafast time scale of the isotope effect experimentally observed.[1, 2] The HHG spectra reported by Madsen et al[10] also confirm the involvement of the same modes.

Results

Our quantum dynamical results reveal that on the cation ground state (GS), the D_{2d} basin is populated before the C_{2v} one. The strong isotopic effect in the early 1-2 fs dynamics is found to be related to electronic coherences and ensuing amplitude transfers from the 1st (S1) and the 2nd (S2) excited states to the GS of the cation. These results are robust against averaging the quantum dynamics over an ensemble of 8000 initial states that span the FC region on the three lowest excited states determined from the sudden ionization of molecules randomly oriented with respect to the polarization of the XUV pulse.

To investigate the dynamics, we solve the time-dependent Schrödinger equation on a 2 dimensional nuclear coordinate system for the three lowest states of the methane cation that

are non adiabatically coupled due to the JT effects (see Computational Methods and the SI for more details). The two coordinates, q_1 and q_2, are defined as a linear combination of Cartesian displacements that lead to the specific C_{2v} (q_1) and D_{2d} (q_2) minima shown in Figure 1B and include small distortions in order to span the NAC seams.

The q_1 coordinate has significant amplitudes on the components of the t_2 and e modes involved in the JT distortion and the q_2 coordinate has components of the e mode (see Table S1 of the SI). In addition both coordinates have small amplitudes on the a_1 mode and on the other t_2 mode of the T_d geometry. Outside of the T_d geometry in the FC region, q_1 and q_2 have amplitudes on the normal modes of the C_{2v} and D_{2d} forms involved in the NAC seams, see Tables S2 and S3 of the SI. The electronic structure at each grid point is computed at the SA-CASSCF (9,8) /6-31G++(2df,2pd) level for the three lowest states of the cation and CASSCF (10,8) /6-31G++(2df,2pd) for the GS of the neutral using MOLPRO.[11] The computed vertical ionization energy to the T_d point is 13.61 eV. On the cation GS, the C_{2v} minima correspond to the lowest energy, the D_{2d} minimum is 0.2837 eV above in agreement with ref.[4]. The three potential energy surfaces (PES) on the 2D grid are shown in Figure 1B (see also Figure S1 for isocontour plots and the Computational Methods section). On the GS, in addition to the two wells that correspond to slightly D_{2d} and C_{2v} geometries at (-1.4,0) and (0,-1.12) respectively, there is also a third minimum close to a C_s symmetry at (1.08,1.26). We describe the geometry on a grid using 146 grid points for q_1 and 184 for q_2 which leads to 26864 grid points per electronic state. See Computational Methods for more details.

The definition of the initial state is a crucial point in determining the short time dynamics resulting from sudden ionization of the GS neutral. Typically, experiments are done for randomly oriented molecules with respect to the polarization of the ionizing pulse. This

requires averaging the quantum dynamics over an ensemble of orientations with respect to the electric field. Another important aspect is to account for the strong variation of the photoionization cross sections to the three electronic states of the cation as a function of the geometry on the FC region of the neutral ground state. The amplitudes of the initial states on the three electronic states of the randomly oriented CH_4^+/CD_4^+ ions are weighted by the amplitude of the neutral vibrational ground state, $c_{GS,g}^{neut}$, on the 2D grid and defined as $c_{ig}^{m} = c_{GS,g}^{neut}\sqrt{\rho(\varepsilon)}\hat{\mathbf{e}}.\mathbf{d}_{ig}^{\varepsilon}$, see Computational Methods for the details. In c_{ig}^{m}, m represents a given orientation, $\hat{\mathbf{e}}_m = \mathbf{E}_m / |E|$, of the electric field of the ionizing pulse with respect to the laboratory frame shown in Figure 1A and *ig* is the index notation for electronic state *i* and grid point *g*. $\mathbf{d}_{ig}^{\varepsilon}$ is the transition dipole from the GS neutral to the continuum of the ith electronic state at grid point *g* integrated over the solid angle $\hat{\Omega}$ with ε the kinetic energy of the photoelectron computed at grid point *ig*. $\rho(\varepsilon)$ is the density of photoelectron states. The norms of the initial states, $|\mathbf{c}_m|^2 = \sum_{ig} |c_{ig}^{m}|^2$ are proportional to the total angularly resolved photoionization yields. The computed photoionization angular maps are plotted for CH_4^+ in Figure 2, separately for each electronic state. The plot is a heatmap on the unit sphere. In order to investigate the role of the multistate dynamics on the isotope effect, we selected two carrier frequencies for the ionizing XUV pulse, corresponding to the 9th and the 11th harmonic produced by HHG with 800nm laser pulse: $h\nu_9$ =13.95 and $h\nu_{11}$ = 17.05 eV respectively. Photoionization by the $h\nu_9$ pulse builds a non stationary wave packet on the cation with 54% population in the GS, 41% in the S1 state and a small amount of population in S2 (5%). On the other hand, all three states of the cation are accessed by the $h\nu_{11}$ which leads to 26% of population in the GS, 37% in S1 and37% in S2. Overall, the total ionization yield for the $h\nu_{11}$

pulse is 14% higher than for $h\nu_9$ one. There is no significant differences in the main features of the angularly resolved yields computed for CD_4^+ shown in Figure S2 of the SI since the energetics of the electronic states is the same for the two ions and the total yields in the three electronic states are in the same ratios. However, the isotope substitution affects the spreading of the ground vibrational state of the neutral which is narrower in the case of CD_4^+. This leads to a smaller extension of the FC region. As we discuss below, this isotope effect has important consequences for the localization of the initial states and on the subsequent multistate dynamics.

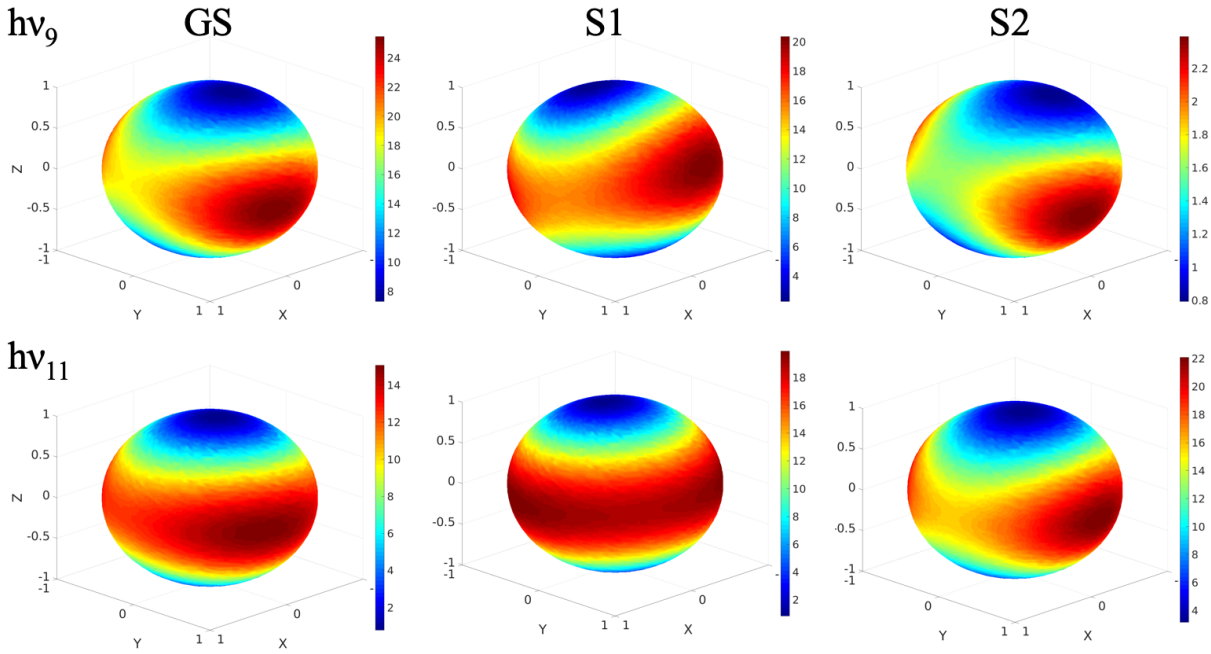

Figure 2 : Heatmaps of the angularly resolved photoionization yields plotted separately for each electronic state ($\sum_g \left|c_{ig}^m\right|^2$ with i = GS, S1 and S2) computed for CH_4^+ and two carrier frequencies of the ionization XUV attopulse ($h\nu_9$ = 13.95 eV and $h\nu_{11}$= 17.05 eV). The heatmaps are computed by drawing 8000 random orientations, $\hat{\mathbf{e}}_m$, of the electric field.

(X,Y,Z) represent the Cartesian coordinates of the unit vector $\hat{\mathbf{e}}_m = \mathbf{E}_m / |\mathbf{E}|$ with respect to the laboratory frame shown in Figure 1A. Note how for the S2 state, the yield is very small for the 9th harmonic while it is comparable to the lowest states for the 11th one. See figure S2 of the SI for the photoionization yields of CD_4^+.

The vectors, $\mathbf{c}_m$, of the initial states on the grid define an ensemble with a density matrix $\rho_{ens}(0)$, $\rho_{ens}(0) = \sum_m^M \rho_m(0) = \sum_m^M \mathbf{c}_m \mathbf{c}_m^\dagger$, which is the sum of the M pure case density matrices, $\rho_m(0)$. M is the number of orientations of the electric field of the ionizing pulse with respect to the laboratory frame shown in Figure 1A. M needs to be quite large in order to get an accurate sampling of the orientations. We use M = 8000 for computing the heatmaps shown in Figure 2 above. We show in the Computational Methods that the $\rho_{ens}(0)$ matrix is very rank deficient and possesses only three non zero eigenvalues. Its spectral representation then takes the form: $\rho_{ens}(0) = \sum_{r=1}^3 \omega_r \mathbf{s}_r \mathbf{s}_r^\dagger$. This feature leads to a considerable saving of computer time for getting an accurate ensemble averaging of the quantum dynamics over orientations. The time evolution of each component, $\rho_m(0)$, of the ensemble density matrix is unitary and therefore the ensemble density matrix, $\rho_{ens}(0)$, will also evolve under a unitary transformation. To describe the ensemble dynamics, it is therefore numerically strictly equivalent to solve the time-dependent Schrödinger equation on the grid for the three eigenvectors $\mathbf{s}_r$, r =1,2,3, of the ensemble density matrix that correspond to a non zero eigenvalue or to solve it for the 8000 $\mathbf{c}_m$ vectors. More details can be found in Computational Methods.

We show in Figure 3 the initial localization in the Franck-Condon region of the diagonal elements of $\rho_{ens}(0)$, $\left[\rho_{ens}(0)\right]_{ig,ig} = \sum_m \left|c_{ig}^m\right|^2 = \sum_{r=1}^3 \omega_r \left|s_{ig}^r\right|^2$ on the 2D grid points g separately for the three electronic states, i = GS, S1 and S2, computed for CH_4^+ for the two wave lengths of the ionizing pulse, $h\nu_9$ in the top row and $h\nu_{11}$ in the bottom one. The localization patterns of the initial state on each electronic state exhibit the same features for the two pulses, but the features obtained for the $h\nu_{11}$ pulse are more spread. The localization of the initial state is asymmetrically distributed along the $q_1 = q_2$ diagonal for the GS and the S2 states. The initial localization on the GS (left column in Figure 3) has a larger extension in the upper diagonal part, towards the D_{2d} minimum at (0,-1.12) in the (q_1,q_2) coordinates, while for the S2 state (right column), the initial state has a larger extension in the lower diagonal part, towards C_{2v} region at (-1.4,0). The localization on the S1 state tends to be more evenly distributed between the two regions. The same patterns are observed for CD_4^+ shown in Figure S3, but overall the initial density is more localized around the T_d region because the CD_4 neutral vibrational ground state is less spread around the T_d geometry due to the mass effect.

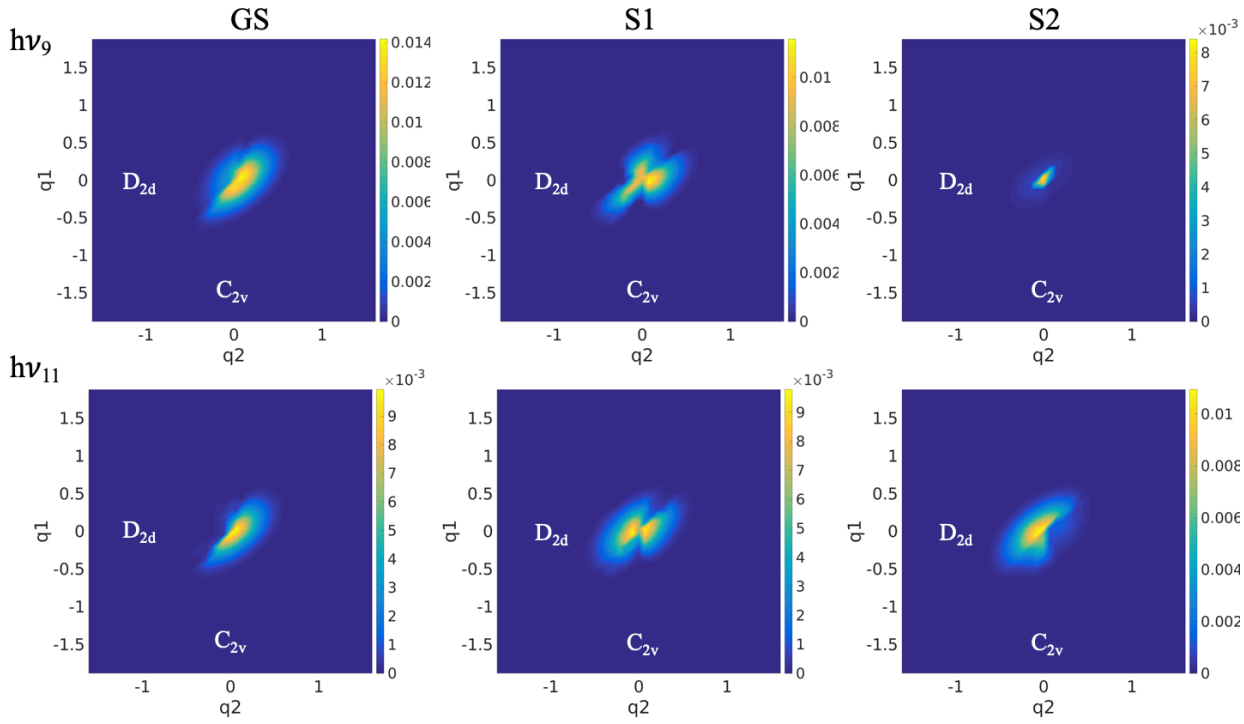

Figure 3 : Heatmaps of the initial population on each grid point, $\left[\rho_{ens}(0)\right]_{ig,ig}$ on each electronic state i = GS (left), S1 (middle) and S2 (right), computed for CH_4^+ for the $h\nu_9$ (top row) and $h\nu_{11}$ (bottom row) pulses. See Figure S3 for CD_4^+.

The time evolution of the total populations in each electronic state averaged over the ensemble are shown in Figures 4A and B for ionization by the $h\nu_9$ and $h\nu_{11}$ pulses respectively, in full lines for CH_4^+ and in dashes for CD_4^+. The GS and S1 states are about equally accessed by the $h\nu_9$ pulse with only a small fraction (5%) in the S2 state. The population transfers between the three states are rather monotonic with very little differences between the two isotopes, and a smooth decay from the S1 state to the GS, while the S2 state remains mostly decoupled from the two lowest ones during the first 24 fs dynamics. On the other hand, for the $h\nu_{11}$ pulse, the three electronic states are about equally accessed by the sudden ionization process. There is a rich non adiabatic dynamics between the three states at early times, with large amplitude oscillations of the populations in S1 and S2 and a more monotonic rise of the population in the

GS. The wave packets are moving over the grid with rates determined by the gradients of the potentials, which, as can be seen from Figure 1B and S1, are very different: The minima on the GS are very shallow. The gradients are larger on S1 and S2. The wells on S1 are deeper and located in the close vicinity of the NAC seam. S2 has a single deep well in the T_d region where the non adiabatic couplings are the largest, see Figure S4. This topology of the S1 and S2 PES favors efficient population transfer from the two higher states to the GS. The oscillations of the populations do not occur with a definite period because of vibrational coherences on each potential and of the complex dynamics of the electronic coherences between the three states shown in Figure S5. The periods of the electronic coherences are given by the energy difference between the two states involved and vary with the localization of the wave packets on the grid. Their amplitudes are modified by the transfers between the states in the NAC regions couplings. Heatmaps of the NAC matrix elements on the grid, $\tau_{ij}(g)$, are shown in Figure S4. One can see that NAC seams form a dense network of regions of efficient amplitude transfer. Overall the periods of the oscillations in the populations plotted in Figure 3B for the $h\nu_{11}$ pulse are about 3 fs in CH_4^+ (full lines) and longer in CD_4^+ (dashes), for which they are between 4 and 6 fs. After ≈ 15 fs, the non adiabatic transfers are more monotonic and the isotopic effect less pronounced. When a wave packet involving several electronic states reaches a NAC region, one can show algebraically that the population transfers are governed by the electronic coherences.[12]. Such a strong isotopic effect on the population transfers due to NAC driven by electronic coherences have already been reported by us for N_2[13, 14, 15] and LiH[16].

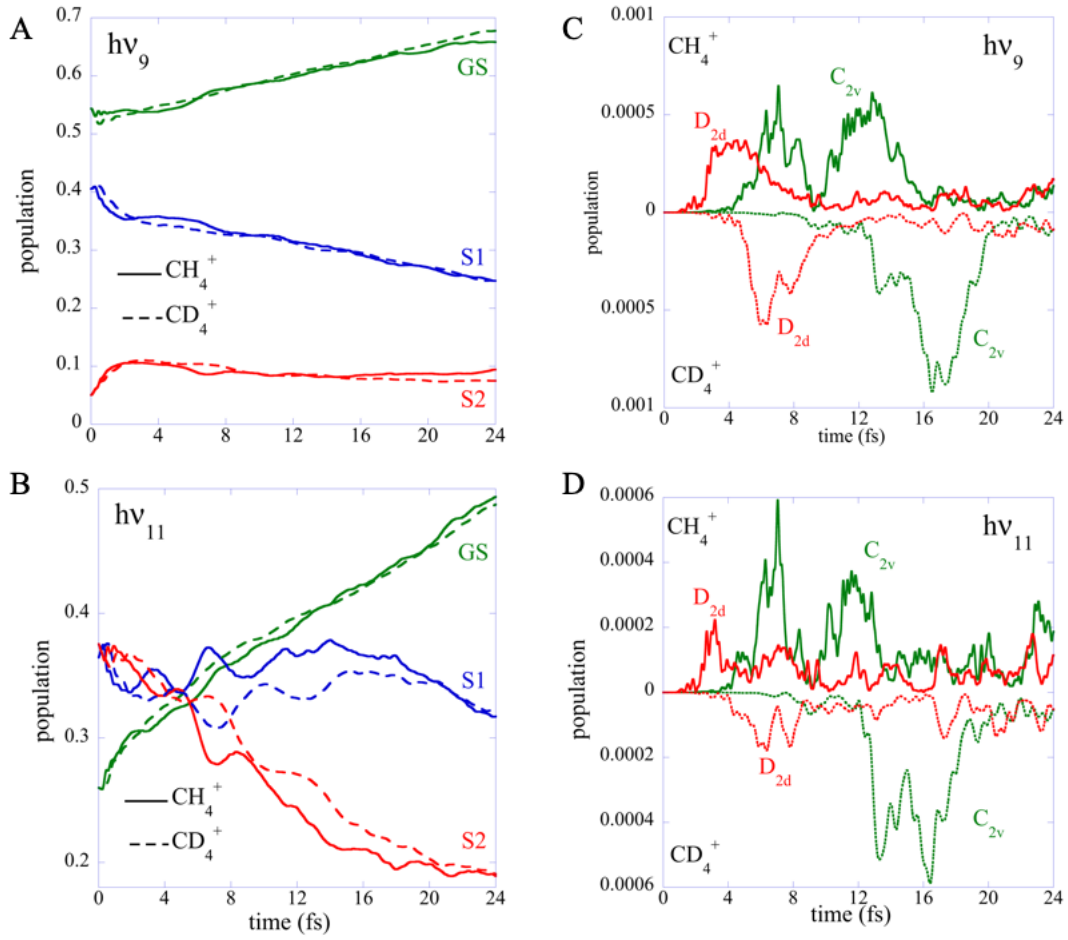

Figure 4: A and B: Early times population dynamics of CH_4^+ (full lines) and CD_4^+(dashes) computed for a sudden ionization with the $h\nu_9$ pulse (panel A) and the $h\nu_{11}$ pulse (panel B) on the three electronic states of the cation (GS : green, S1: blue and S2: red). C and D : populations of the grid point corresponding to the D_{2d} (red) and C_{2v} (green) minima of the GS computed for CH_4^+ and CD_4^+ with the $h\nu_9$ pulse (panel C) and the $h\nu_{11}$ pulse (panel D). Movies of the localization of the wave packet on the three electronic states are available in the SI.

The time scale and the efficiency of the transfers to the D_{2d} and C_{2v} regions of the GS on the grid result from the interplay between the localization of the initial states shown in Figure 2,

the motion of the wavepackets on the ground state of the cation and the network of NAC seams shown in Figure S4 that allow transfer from S1 and the S2 states. As we show in Figure 2, the localization of the initial state on the GS state is skewed towards the D_{2d} region while it is more evenly spread for S1 and skewed to the C_{2v} in S2. On the other hand, the localization of the network of NAC seams (Figure S4) does not favor one minimum or the other.

The populations of the grid points that correspond to the C_{2v} and D_{2d} minima of the GS are plotted in Figure 4 C and D for ionization by the $h\nu_9$ and the $h\nu_{11}$ pulses respectively. One clearly sees that the D_{2d} minimum (red) is visited first by the wave packet with a maximum at 4 fs for CH_4^+ and 7fs for CD_4^+. This occurs before the rise in the C_{2v} minimum grid point and the concomitant decay in the D_{2d} one. One does not observe a significant difference in the rise of population in the D_{2d} minimum for ionization by the $h\nu_9$ or the $h\nu_{11}$ pulses, which suggests that the early population of the D_{2d} minimum results from the GS dynamics. This is supported by the fact that comparatively, the maximum of population in the D_{2d} minimum is about half for the $h\nu_{11}$ pulse (figure 4D) than for the $h\nu_9$ in agreement with the smaller population in the GS for an ionization by the $h\nu_{11}$ pulse. The respective rise in the D_{2d} and C_{2v} minima are delayed for CD_4^+ at ≈5fs and ≈12-13fs compared to ≈ 1.5 fs and 5fs for CH_4^+. We show in Figure S6 the populations computed in larger regions (25 points) around the two minima which represent ≈5 to 10% of the population in the GS. For these larger regions, the population in the D_{2d} regions clearly rises before that in C_{2v} region too. For completeness, in figure S6, we also added the population in a region of 25 grid points in the C_s minimum. One can see that the onset of the rise of population in this minimum is intermediate between that of the $D_{2}d$ and C_{2v}.

The square moduli of the autocorrelation function of the initial state, $|C(t)|^2_{\mathrm{H}}$ and $|C(t)|^2_{\mathrm{D}}$, are plotted in Figure 5A. As expected because of the mass difference, the initial decay of $|C(t)|^2_{\mathrm{D}}$

is slower than that of $|C(t)|^2_H$ and the decay rates out of the initial state are very similar for the two pulses up to 1.5 fs. After 3 fs, the initial decay is over and the overlap of the wave packet with its initial location is very small. The ratio $|C(t)|_D^2 / |C(t)|_H^2$ governs the yield in harmonics.[1, 2, 3] It is plotted in Figure 5B from 1 to 1.6 fs, the time range for which the experimental harmonic yield ratio was reported in ref. [1]. For the $h\nu_{11}$ pulse, the computed ratio (orange) is in excellent agreement the ratio of the yields in high harmonics reported in ref. [1]. It is equal to 1.7 at 1 fs compared to an experimental value of the ratio of harmonic yields of 1.75 and at 1.6 fs , the computed ratio is 2.6 compared to a value of 3 for the ratio of the harmonic yields. The agreement is less good for ionization by the $h\nu_9$, with a computed value of ≈ 1.5 for the entire range [1,1.6] fs. This suggests that the very early time non equilibrium electronic dynamics involving the three electronic states of the cation plays a crucial role in leading to the large isotope effect at short times. The faster rise of the computed $|C(t)|_D^2 / |C(t)|_H^2$ ratio for the $h\nu_{11}$ in the range 1 to 2 fs and its larger amplitude oscillations at 2, 4.5 and 8 fs (Figure 5C) can be traced to the large amplitude of the GS-S1, GS-S2 and S1-S2 electronic coherences shown in Figure S5 which are delayed for CD_4^+ compared to CH_4^+. Since for an ionization by $h\nu_{11}$ pulse, there are similar amounts of population in the three states, the fast oscillations of the GS-S2 coherence in particular have a large amplitude. The longer period of the GS-S2 coherence in CD_4^+ leads to the maxima at 2 and 4.5fs in the $|C(t)|_D^2 / |C(t)|_H^2$ ratio (figure 5C) while there is only one broad peak with a max at 3 fs for the ionization by the $h\nu_9$ pulse. The first fast oscillations of the GS-S2 coherence also plays a role in the first 2 fs of the dynamics of the decay of the autocorrelation functions of the two isotopes, as can be seen in figure S7 where the contributions of the diagonal and off diagonal terms of the electronic coherences to the square modulus,

$$\left|C(t)\right|^2 = \sum_{i=1}^{3} \sum_{gg'} c_{ig}^{*}(0) c_{ig}(t) c_{ig'}^{*}(0) c_{ig'}(t) + \sum_{i,j\neq i}^{3} \sum_{gg'} c_{ig}^{*}(0) c_{ig}(t) c_{jg'}^{*}(0) c_{jg'}(t)$$

, are plotted separately. One can see from Figure S7 that the higher ratio, $|C(t)|_D^2$ / $|C(t)|_H^2$ is due to the GS-S2 coherence term which decays faster for CH_4^+ than for CD_4^+. This coherence does not contribute much to $\left|C(t)\right|^2$ in the case of ionization with the $h\nu_9$ pulse, since the population in the S2 state is very small. The values of the ratios including and not including the GS-S2 and S1-S2 coherence terms in the autocorrelation functions shown in figure S8 confirm the role of electronic coherences involving the S2 state in the isotope effect. Snapshots of the localization of the real part of the GS-S2 electronic coherence, $\rho_{02,g}(t)$, on the grid are plotted in Figure 5D for CH_4^+ and CD_4^+ for ionization by the $h\nu_{11}$ pulse. One clearly sees the faster delocalization of the GS-S2 electronic coherence to the D_{2d} region by ≈ 1.6 fs for CH_4^+ while it has hardly moved out of the FC region for CD_4^+. Movies of the localization of the GS-S1 and S1-S2 electronic coherences on the grid are available in the SI. They also visit the D_{2d} region at very short time, before 4fs.

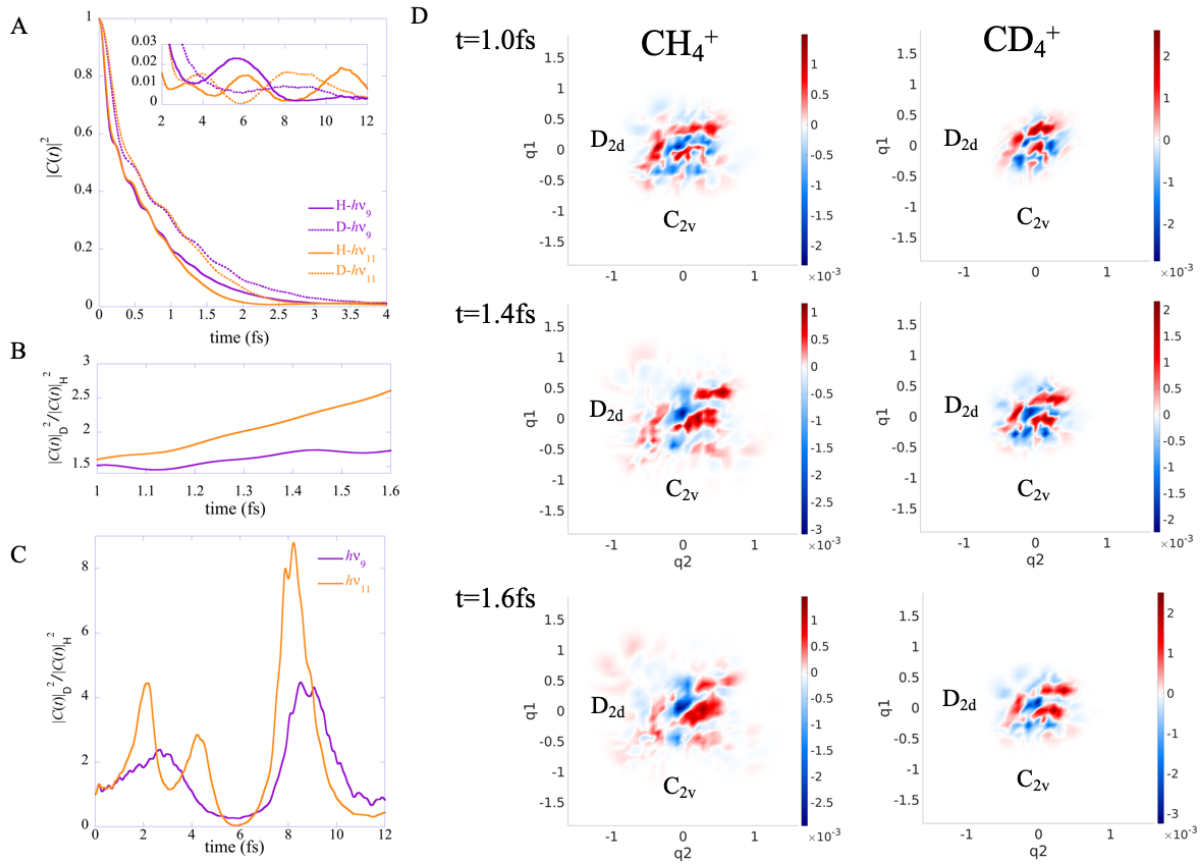

Figure 5: A. The square modulus of autocorrelation function, $|C(t)|2$ computed for the $h\nu_9$ pulse in violet and for the $h\nu_{11}$ in orange, CH_4^+ in full lines and CD_4^+ in dotted lines. The inset shows the small recurrences at longer times. B. The ratio $|C(t)|_D^2/|C(t)|_H^2$ for the $h\nu_9$ (violet) and the $h\nu_{11}$ pulse (orange) at short time. C. The ratio $|C(t)|_D^2/|C(t)|_H^2$ at longer times. D. Snapshots of the localization of the real part of the GS-S2 electronic coherence, left CH_4^+, right CD_4^+ computed for the $h\nu_{11}$ pulse. Note how the GS-S2 coherence delocalizes towards D_{2d} for CH_4^+ while it has not migrated yet out of the FC region for CD_4^+. Movies of the localization of the GS-S1,GS-S2 and S1-S2 electronic coherences are available in the SI.

Discussion

A sudden ionization produces a methane cation at the equilibrium geometry of the neutral as a coherent superposition of three distinct electronic states. These adiabatic states are coupled by a Jahn-Teller distortion. Quantum mechanical dynamical computations on accurate potential

energy surfaces and couplings show that electronic coherences play a key role in the early time evolution of the coupled electronic—nuclear states. This results in a significant isotopic difference between CH_4^+ and CD_4^+. The magnitude of the effect is comparable to that reported experimentally using high harmonic generation spectroscopy. [1] The results are robust with respect to the orientation of the molecule with respect to the polarization of the electric field of the ionizing pulses. The dynamics are computed by averaging over an ensemble of 8000 different initial conditions corresponding to the orientation of the neutral molecule with respect to the laser pulse. There are however just three principal components to that ensemble and propagating them allows for a computationally efficient implementation.

The strong isotopic effect in the early 1-2 fs dynamics is shown to be related to electronic coherences that govern the amplitude transfers from the S1 and the S2 excited states of the cation to its GS. On the ground state the shallow basin around the less distorted D_{2d} geometry is accessed first and is followed by a rearrangement to the C_{2v} geometry where both the bonds and the angles are modified. The D_{2d} geometry is established by about 4fs for CH_4^+ and at 8fs CD_4^+. Primarily this is due to the variation of the photoionization matrix elements with the geometry of the ground state in the Franck-Condon region that lead to different localization of the initial state resulting from the sudden ionization process. Such ultrafast electronic and structural rearrangements in cations ionized to multiple interfering channels are ideally probed by HHG spectroscopy [17, 18] which provides the needed sub to few fs time resolution. Recent developments in 3D two electron angular streaking[19] and time-resolved X-Ray Transient Absorption spectroscopy[20, 21] could also shed light on such ultrafast processes.

Computational Methods

Definition of the coordinates of the grid

CH_4^+ possesses 9 internal coordinates. They are all involved in the configurational distortions leading to the C_{2v} and D_{2d} minima on the ground state of the cation and in the non adiabatic coupling seams between the three lowest excited states. In order to capture the main features of the early time non adiabatic quantum dynamics, we define a grid with two coordinates, q_1 and q_2, that are linear combinations of 15 Cartesian displacements $\Delta_{i\alpha}$:

$$q_1 = \sum_{i=1}^{5} \sum_{\alpha=1}^{3} a_{i\alpha}\Delta_{i\alpha} \qquad (1)$$

$$q_2 = \sum_{i=1}^{5} \sum_{\alpha=1}^{3} b_{i\alpha}\Delta_{i\alpha} \qquad (2)$$

with α = 1, 2,3 for the three Cartesian displacements $\Delta_{i\alpha}$ on each atom.

Table 1: Normalized Cartesian displacements defining the two coordinates q_1 and q_2

	Δx_C	Δy_C	Δz_C	Δx_{H1}	Δy_{H1}	Δz_{H1}	Δx_{H2}	Δy_{H2}	Δz_{H2}
q_1	0.00547	-0.00554	0.09994	0.35209	0.31586	-0.49586	-0.38280	-0.28470	-0.49588
q_2	0.00550	-0.00557	0.00080	-0.17315	-0.20960	0.41467	0.14224	0.24096	0.41464
	Δx_{H3}	Δy_{H3}	Δz_{H3}	Δx_{H4}	Δy_{H4}	Δz_{H4}			
q_1	-0.05665	0.12396	-0.09771	0.02220	-0.08911	-0.10147			
q_2	-0.17478	0.24251	-0.41752	0.14011	-0.20744	-0.42131			

The coordinate q_1 points to the C_{2v} minimum of the GS cation while the coordinate q_2 points to the D_{2d} minimum. In addition, the Cartesian displacements Δ_i include distortions that allow spanning the NAC's seams between the three lowest states. On the grid, the point closest to a C_{2v} minimum on the ground state is at $q_1 = -1.4$ and $q_2 = 0$. It has a root mean square deviation (RMSD) of 0.0418 Bohr compared to the C_{2v} geometry. Strictly speaking, if there was no distortion and all the grid points were of C_{2v} symmetry, a second C_{2v} minimum should be

present on the grid. However, maintaining the C_{2v} geometry for all grid points leads to zero non adiabatic coupling by symmetry. The other minimum on the grid corresponds to more distorted C_{2v} geometry with a RMSD of 0.1384 Bohr with respect to C_{2v}, that is actually closer to a C_s symmetry. It is located at q_1=1.08 and q_2=1.26 and 0.1583 eV above the C_{2v} minimum on the grid. The D_{2d} minimum on the grid is localized at q_1= 0 and q_2 =-1.12 at a relative energy of 0.165 eV compared to the minimum C_{2v} on the grid. The RMSD from a D_{2d} geometry is 0.0321 Bohr. On the GS, the gradients from the T_d point on the grid in the directions of these three minima are nearly identical. The S1 PES on the grid exhibits three minima, localized close to the GS/S1 seams. There is a single well localized around T_d for S2 PES. Isocontours of the 3 PES are plotted in Figure S1. The size of the grid is defined to avoid reflections of the wave packet on the edges for the time range investigated . The grid extends from -5.8 to + 5.8 by step of 0.08 for q_1 and from -7.98 to 4.83 with a step 0.07 for q_2, which leads to 26864 grid points per electronic state. The FC region is defined by the ground vibrational state of the neutral at its equilibrium geometry. The D_{2d} and C_{2v} minima are located on the edges of the FC region which is centered on the Td geometry and comprises 1886 grid points. There is also C_{3v} minimum on the GS PES whose geometry falls outside the grid but whose computed energy and geometry are in agreement with ref. [4]. We give in Tables S1 to S3 of the SI the decomposition of the two coordinates on the normal modes of the T_d, C_{2v} and D_{2d} geometries of the GS of the cation. The position of the center of mass is conserved for all the geometries sampled by the grid.

Vibronic Hamiltonian on the grid

We use atomic units throughout. In the (q_1, q_2) coordinates, the kinetic energy operator takes the form :

$$\hat{T} = -\frac{1}{2}\left(\frac{1}{\mu_1}\frac{\hat{\partial}^2}{\partial q_1^2} + \frac{1}{\mu_2}\frac{\hat{\partial}^2}{\partial q_2^2} + \frac{1}{\mu_{12}}\frac{\hat{\partial}^2}{\partial q_1 \partial q_2}\right)$$
$$\mu_1^{-1} = \sum_i \frac{1}{m_i}\sum_\alpha^3 a_{i\alpha}^2, \quad \mu_2^{-1} = \sum_i \frac{1}{m_i}\sum_\alpha^3 b_{i\alpha}^2, \quad \mu_{12}^{-1} = \sum_i \frac{1}{m_i}\sum_\alpha^3 b_{i\alpha}a_{i\alpha} \tag{3}$$

with m_i being the mass of C and H respectively.

The Hamiltonian includes the non adiabatic coupling between the three lowest electronic states of the cation. The basis functions are the product of the adiabatic electronic wave function of state i, $\left|\Psi_{ig}^{elec}\right\rangle$, computed at the grid point g which corresponds to a value of q_1 and q_2 and a product of orthonormal window functions $\theta_g = \theta\left(q_{1g}\right)\theta\left(q_{2g}\right)$ centered at each grid point. In short notation we denote the full wave function at each grid point $\left|ig\right\rangle$. After integration on the electronic coordinates, the matrix elements of the Hamiltonian between two basis wave functions $\left|ig\right\rangle$ and $\left|jg'\right\rangle$ take the form:

$$\mathbf{H}_{ig,jg'}(t) = -\frac{1}{2}\mathbf{T}_{ig,jg'}\delta_{ij} + \mathbf{V}_{ig,jg'}\delta_{ij}\delta_{gg'} + \left(\frac{1}{i}\tau_{ig,jg}\delta_{gg'}\right).\mathbf{p}_{jgg'} \tag{4}$$

where i and j stand for the electronic state index and g and g' for the indices of grid points. $\mathbf{T}_{ig,jg'}$ are the matrix elements of the kinetic energy operator defined in Eq.(3), they are diagonal in the electronic state index but off diagonal in the grid point index. $\mathbf{V}_{ig,jg'}$ are the matrix elements of the potential energy, diagonal in both the electronic and grid indexes.

The non adiabatic coupling (NAC) matrix elements are computed at each grid point, using the quantum chemistry program MOLPRO.[11] $\boldsymbol{\tau}_{ig,jg}$ is the NAC vector expressed in the coordinates $\left(q_1, q_2\right)$, see Figure S4 for a heatmap of the two components on the grid. It is diagonal in the grid point index, g, but off diagonal in the electronic state index. We neglect in Eq. (4) the second derivative matrix elements with respect to the nuclear coordinate of the

electronic wave function. $\mathbf{p}_{jgg'}$ is the matrix of the momentum operator on state j with $\hat{p}_1 = -i\left(\partial/\partial q_1\right)$ and $\hat{p}_2 = -i\left(\partial/\partial q_2\right)$.

The time-dependent Schrödinger equation

$$i\frac{d\mathbf{c}}{dt} = \mathbf{H}\mathbf{c} \qquad (5)$$

is integrated numerically for a vector of amplitudes, **c**, of $L=N$g x 3 =80592 complex components. The action of the non local kinetic energy is computed using a finite difference scheme with $O\left(h^4\right)$ error.[13, 22] We use a $O\left(h^6\right)$ for the momentum operator to retain a good numerical precision in the integration of the terms due to the NAC coupling.

The first-order derivatives are computed at order 6 as [23].

$$\frac{dc_{u,v}}{du} = \frac{1}{60du}\left(-c_{u-3,v} + 9c_{u-2,v} - 45c_{u-1,v} + 45c_{u+1,v} - 9c_{u+2,v} + c_{u+3,v}\right), \quad u, v = q_1, q_2 \qquad (6)$$

where u and v represents the q_1 and q_2 coordinates corresponding to a grid point g. The second order derivatives are given by[23]:

$$\frac{d^2c_{u,v}}{du^2} = \frac{1}{12du^2}\left(-c_{u-2,v} + 16c_{u-1,v} - 30c_{u,v} + 16c_{u+1,v} - c_{u+2,v}\right) \qquad (7)$$

and the cross derivatives between the two internal coordinates v and u:

$$\frac{dc_{u,v}}{dvdu} = \frac{1}{2dvdu}\left(-c_{u,v+1} - c_{u,v-1} - c_{u+1,v} - c_{u-1,v} + c_{u-1,v-1} + c_{u+1,v+1} + 2c_{u,v}\right) \qquad (8)$$

The amplitudes $c_{ig}\left(t\right)$ are propagated using Eq. (5) using a time step of 0.01 a.u. of time and a 4th order Runge-Kutta scheme for the time integration which allows to keep the norm up to 10^{-8} for the time range of 50 fs investigated.

Initial density matrix of the ensemble.

We draw an ensemble, a mixture of 8000 initial states, with random orientations, $\hat{\mathbf{e}}$, of the electric field with respect to the molecular frame. For each orientation, $\hat{\mathbf{e}}$, and each carrier frequency, $h\nu_9$ or $h\nu_{11}$, of the ionizing pulse, we define a vector, $\mathbf{c}_m$, of complex amplitudes, c_{ig}^m, on the grid points $\left(q_1,q_2\right)$ for each electronic state *i*, *i* =1, 2, 3 :

$$c_{ig}^m = c_{GS,g}^{neut}\sqrt{\rho\left(g,\varepsilon\right)}\hat{\mathbf{e}}_m.\mathbf{d}_{ig}^{\varepsilon} \tag{9}$$

where *m* is the index for the initial conditions, $\hat{\mathbf{e}}_m$, for a given value of the carrier frequency of the pulse and *ig* is the electronic state-grid index. $\rho\left(g,\varepsilon\right)$ is the density of states computed at grid point *g* for an ionization for electronic state *i*.

The $\mathbf{d}_{ig}^{\varepsilon}$ are the photoionization matrix elements from the GS neutral to the three electronic states of the cation at each grid point integrated over the solid angle $\hat{\Omega}$:

$$\mathbf{d}_{ig}^{\varepsilon} = \sqrt{2}\int d\hat{\Omega}\int d\mathbf{r}\phi_{GS-ig}^{D}\left(\mathbf{r}\right)\mathbf{r}\,\phi_{\varepsilon,\hat{\Omega}}^{elec\perp}\left(\mathbf{r}\right) \tag{10}$$

The $\mathbf{d}_{ig}^{\varepsilon}$'s are computed within the sudden ionization approximation for each grid point in the FC region as described in ref. [24]. The kinetic energy of the photoelectron at each grid point and each electronic state is defined as $\varepsilon = h\nu - \left(V_{ig}^{cat} - V_{GSg}^{neut}\right)$ for a given carrier frequency, $h\nu$, of the XUV pulse. $\phi_{GS-ig}^{D}\left(\mathbf{r}\right)$ is the Dyson orbital between the GS of the neutral and the electronic state *i* of the cation computed at grid point *g* at the CASSCF (10,8) and SA3-CASSCF (9,8) levels with the atomic basis set /6-31G++(2df,2pd) respectively. The photoelectron wave functions, $\phi_{\varepsilon,\hat{\Omega}}^{elec\perp}\left(\mathbf{r}\right)$, are orthogonalized plane waves with $\varepsilon = k^2/2$, for

the wave vector **k**. The photoelectron continuum is discretized in 256 *k* values. For each *k* value, an ensemble of 512 values of solid angles are sampled uniformly on the unit sphere.

The norms of the vectors $\left|\mathbf{c}_m\right|^2 = \sum_{ig} \left|c_{ig}^m\right|^2$, are the ionization yields normalized to the strength of the electrical field, $P_{h\nu,\hat{\mathbf{e}}}$, of the neutral in the direction $\hat{\mathbf{e}}$ for a carrier frequency $h\nu$, shown in Figure 2 of the main text for CH_4^+ and in Figure S1 for CD_4^+. Each vector $\mathbf{c}_m$ defines a pure state and the corresponding *L* by *L* density matrix, $\rho_m(0)$, takes the form:

$$\rho_m(0) = \mathbf{c}_m \mathbf{c}_m^\dagger \tag{11}$$

The ensemble density matrix, $\rho_{ens}(0)$ at time $t = 0$, is the sum of the matrices $\rho_m(0)$:

$$\rho_{ens}(0) = \sum_{m=1}^{M} \rho_m(0) = \sum_{m=1}^{M} \mathbf{c}_m \mathbf{c}_m^\dagger \tag{12}$$

where *M* is the number of orientations of the electric field. Both the density matrix, $\rho_m(0)$, Eq. (11), of a particular orientation, $\hat{\mathbf{e}}_m$, of the electric field in the laboratory frame and the ensemble density matrix, $\rho_{ens}(0)$, Eq. (12), can be written as a quadratic form. Each matrix $\rho_m(0)$ is a pure case of rank 1. For $\rho_{ens}(0)$ one can define a rectangular matrix **A**, of dimensions *L* x *M*, made of the *M* vectors $\mathbf{c}_m$, so that it takes the form

$$\rho_{ens}(0) = \mathbf{A}\mathbf{A}^\dagger \tag{13}$$

For the case studied here, we have that *M*, the number of random orientations of the electric field is much smaller than *L* the number of grid points in 2D multiplied by the number of electronic states. We expect that $M << L$ will typically be the case when averaging over orientations in the case of a multistate quantum dynamics on a multidimensional grid. One can then apply a singular value decomposition (SVD) on the matrix **A** directly:

$$\mathbf{A} = \mathbf{S}\Sigma\mathbf{V}^\dagger \tag{14}$$

where **S** is a L x M matrix of the complex left eigenvectors of **A**, Σ the M x M diagonal matrix of its eigenvalues and the columns of M x M matrix **V** are the complex right eigenvectors. One can show that $\rho_{ens}(0)$ has at most M non zero eigenvalues that are given by the squares of the M eigenvalues of the matrix **A**. The eigenvectors of the $\rho_{ens}(0)$ that correspond to its non zero eigenvalues are the M left eigenvectors of the **A** matrix given by the matrix **S** in Eq. (14) above. The SVD decomposition of the L by M **A** therefore provides a computationally less demanding route than diagonalizing the Hermitian L x L $\rho_{ens}(0)$ density matrix, since we have $M << L$.

In the case of a random orientation of the electric field in the laboratory frame, one can show analytically that there are only three non zero eigenvalues of the matrix **A**, which leads to a very large saving of computer time for computing the time evolution of the ensemble.

From Eqs. (9) and (10), one can define a transition dipole vector at each grid point weighted by the amplitude of the neutral ground state, $c_{GS,g}^{neut}$:

$$\overline{\mathbf{d}}_{ig} = c_{GS,g}^{neut}\sqrt{\rho(\varepsilon)}\mathbf{d}_{ig}^{\varepsilon} \tag{15}$$

so that we can rewrite the amplitude of the initial state on the grid (Eq. (9)) as

$$c_{ig}^{m} = \hat{\mathbf{e}}_m^T.\overline{\mathbf{d}}_{ig} \tag{16}$$

Using this notation, one matrix element *ig,jg'* of L x L $\rho_{ens}(0)$ in Eq. (12) takes the form

$$\begin{aligned}\rho_{ens}^{ig,jg'} &= \sum_m \left(\hat{\mathbf{e}}_m^T.\overline{\mathbf{d}}_{ig}\right)^{\dagger}\left(\hat{\mathbf{e}}_m^T.\overline{\mathbf{d}}_{jg'}\right) = \sum_m \left(\overline{\mathbf{d}}_{ig}^{\dagger}.\hat{\mathbf{e}}_m\right)\left(\hat{\mathbf{e}}_m^T.\overline{\mathbf{d}}_{jg'}\right) \\ &= \overline{\mathbf{d}}_{ig}^{\dagger}\left(\sum_m \hat{\mathbf{e}}_m\hat{\mathbf{e}}_m^T\right)\overline{\mathbf{d}}_{jg'}\end{aligned} \tag{17}$$

where the normalized vectors $\hat{\mathbf{e}}_m$ have each 3 Cartesian components : $\hat{\mathbf{e}}_m = \begin{pmatrix} X_m & Y_m & Z_m \end{pmatrix}^T$. The matrix $\sum_{m=1}^{M} \hat{\mathbf{e}}_m.\hat{\mathbf{e}}_m^T$ is a 3x3 matrix which for random

orientations of the vectors $\hat{\mathbf{e}}_m$ is diagonal and is a multiple of the unit matrix by a constant that depends on the number of samplings, *M*. It can therefore be factorized in front of the row vector $\overline{\mathbf{d}}_{ig}^{\dagger}$ in Eq. (17). Since each column vector $\overline{\mathbf{d}}_{ig} = \begin{pmatrix} \overline{d}_{ig}^{X} & \overline{d}_{ig}^{Y} & \overline{d}_{ig}^{Z} \end{pmatrix}^{T}$ has three Cartesian components, the expression of the full matrix $\rho_{ens}(0)$ given in Eq. (12) and Eq. (13) becomes is a *L* x *L* matrix that is the product of the *L*x3 matrix $\overline{\mathbf{d}}^{\dagger}$ and the 3x*L* matrix $\overline{\mathbf{d}}$. So in case of a random orientation of the electric field with respect to the molecular frame, the quadratic form of $\rho_{ens}(0)$ in Eq. (13) takes a simpler form where the matrix **A** is replaced by the matrix $\overline{\mathbf{d}}$:

$$\rho_{ens}(0) = \overline{\mathbf{d}}^{\dagger}\overline{\mathbf{d}} = \begin{pmatrix} \overline{d}_1^X & \overline{d}_1^Y & \overline{d}_1^Z \\ \vdots & \vdots & \vdots \\ \\ \overline{d}_L^X & \overline{d}_L^Y & \overline{d}_L^Z \end{pmatrix} \begin{pmatrix} \overline{d}_1^X & \cdots & \overline{d}_L^X \\ \overline{d}_1^Y & \cdots & \overline{d}_L^Y \\ \overline{d}_1^Z & \cdots & \overline{d}_L^Z \end{pmatrix}^{*} \qquad (18)$$

$\rho_{ens}(0)$ is therefore of rank 3 and its spectral representation takes the form :

$$\rho_{ens}(0) = \sum_{r=1}^{3} \omega_r^2 \mathbf{s}_r \mathbf{s}_r^{\dagger} \qquad (19)$$

where the eigenvectors $\mathbf{s}_r$ are complex and orthonormal. The eigenvectors of $\rho_{ens}(0)$ that correspond to a non zero eigenvalue are given by the left eigenvectors of the SVD decomposition of the matrix $\overline{\mathbf{d}}$ in Eq. (18) :

$$\overline{\mathbf{d}} = \mathbf{S}_{\mathbf{d}} \Sigma_{\mathbf{d}} \mathbf{V}_{\mathbf{d}}^{\dagger} \qquad (20)$$

$\mathbf{S}_{\mathbf{d}}$ is the *L* x 3 matrix of the left eigenvectors of $\overline{\mathbf{d}}$, the three $\mathbf{s}_r$ eigenvectors of $\rho_{ens}(0)$. $\Sigma_{\mathbf{d}}$ is the 3 x 3 matrix of the eigenvalues and $\mathbf{V}_{\mathbf{d}}^{\dagger}$ is the 3x3 matrix of the right eigenvectors. The

eigenvalues of $\rho_{ens}(0)$ are given by the squares of the eigenvalues of $\overline{\mathbf{d}}$. To compute the time evolution of the density matrix of the ensemble, it is therefore strictly equivalent to either propagate the M=8000 $\mathbf{c}_m$ vectors or to propagate the three $\mathbf{s}_r$ vectors using the time dependent Schrödinger equation (Eq. (5)). This is because the time evolution of $\rho_{ens}(0)$ is unitary and dictated by the Hamiltonian (Eq. (4)). Diagonalizing the $\overline{\mathbf{d}}$ matrix by SVD and propagating its left eigenstates therefore provides a considerable saving of computer times and allows running quantum dynamics for an accurate sampling of the random initial orientations. We checked numerically that it was indeed the case. In general, even if the orientation of the orientations of the electric field in the laboratory frame are not random, diagonalizing the A matrix of Eq. (14) provides a saving of computer time as long as $M << L$ because $\rho_{ens}(0)$ is rank deficient and can have at most M non zero eigenvalues.

The three eigenvalues of $\overline{\mathbf{d}}$ are not equal, which can be understood because the cartesian components of the photoionization matrix elements $\mathbf{d}_{ig}^{\varepsilon}$ are no equal and depend on the grid point g and on the electronic state i. For a given carrier frequency of the XUV ionizing pulse, the traces of $\overline{\mathbf{d}}$ reported in Table S4 are almost identical for CH_4^+ and CD_4^+. The eigenvalues of $\overline{\mathbf{d}}$ and its traces are reported in Table S4, as well as the trace of $\rho_{ens}(0)$ for the four computations. Each $\mathbf{s_r}$ vector has amplitudes on the three electronic states. The three right eigenvectors are localized along the X, Y, and Z directions.

References

1. Baker S, *et al*. Probing Proton Dynamics in Molecules on an Attosecond Time Scale. *Science* **312**, 424 (2006).

2. Marangos JP, Baker S, Kajumba N, Robinson JS, Tisch JWG, Torres R. Dynamic imaging of molecules using high order harmonic generation. *Physical Chemistry Chemical Physics* **10**, 35-48 (2008).

3. Lein M. Attosecond Probing of Vibrational Dynamics with High-Harmonic Generation. *Phys Rev Lett* **94**, 053004 (2005).

4. Frey RF, Davidson ER. Potential energy surfaces of CH+4. *J Chem Phys* **88**, 1775-1785 (1988).

5. Mondal T, Varandas AJC. Structural evolution of the methane cation in subfemtosecond photodynamics. *J Chem Phys* **143**, 014304 (2015).

6. Mondal T, Varandas AJC. On Extracting Subfemtosecond Data from Femtosecond Quantum Dynamics Calculations: The Methane Cation. *J Chem Theory Comput* **10**, 3606-3616 (2014).

7. Mondal T, Varandas AJC. The Jahn-Teller effect in the triply degenerate electronic state of methane radical cation. *J Chem Phys* **135**, 174304 (2011).

8. Patchkovskii S. Nuclear Dynamics in Polyatomic Molecules and High-Order Harmonic Generation. *Phys Rev Lett* **102**, 253602 (2009).

9. Köppel H, Domcke W, Cederbaum LS. Multimode Molecular Dynamics Beyond the Born-Oppenheimer Approximation. In: *Advances in Chemical Physics* (eds Prigogine I, Rice SA). Wiley (1984).

10. Madsen CB, Abu-samha M, Madsen LB. High-order harmonic generation from polyatomic molecules including nuclear motion and a nuclear modes analysis. *Phys Rev A* **81**, 043413 (2010).

11. Werner H-J, Knowles PJ, Knizia G, Manby FR, Schütz M. Molpro: a general-purpose quantum chemistry program package. *Wiley Interdisciplinary Reviews: Computational Molecular Science* **2**, 242-253 (2012).

12. Ben-Nun M, Levine RD. Short-time dynamics on several electronic states: formalism and computational study of I2 in rare gas solvents. *ChemPhys* **201**, 163-187 (1995).

13. Jayantha SA, Komarova KG, Wildenberg Svd, Remacle F, Levine RD. AttoPhotoChemistry: Coherent Electronic Dynamics and Nuclear Motion. In: *Attosecond Molecular Dynamics* (eds Vrakking MJJ, Lepine F). Royal Society of Chemistry (2018).

14. Ajay JS, Komarova KG, Remacle F, Levine RD. Time-dependent view of an isotope effect in electron-nuclear nonequilibrium dynamics with applications to N2. *Proc Natl Acad Sci USA* **115**, 5890-5895 (2018).

15. Komarova KG, Remacle F, Levine RD. Time resolved mechanism of the isotope selectivity in the ultrafast light induced dissociation in N2. *J Chem Phys* **151**, 114308 (2019).

16. Komarova K, vandenWildenberg S, Remacle F, Levine RD. Correlated electron-nuclear motion during non-adiabatic transitions in LiH and its isotopomers. *Journal of Physics B: Atomic, Molecular and Optical Physics* **53**, 134001 (2020).

17. Nisoli M, Decleva P, Calegari F, Palacios A, Martín F. Attosecond Electron Dynamics in Molecules. *Chem Rev* **117**, 10760-10825 (2017).

18. Li J, *et al*. Attosecond science based on high harmonic generation from gases and solids. *Nature Communications* **11**, 2748 (2020).

19. Winney AH, *et al*. Disentangling Strong-Field Multielectron Dynamics with Angular Streaking. *J Phys Chem Lett* **9**, 2539-2545 (2018).

20. Geneaux R, Marroux HJB, Guggenmos A, Neumark DM, Leone SR. Transient absorption spectroscopy using high harmonic generation: a review of ultrafast X-ray dynamics in molecules and solids. *Philosophical Transactions of the Royal Society A: Mathematical, Physical and Engineering Sciences* **377**, 20170463 (2019).

21. Timmers H, *et al*. Disentangling conical intersection and coherent molecular dynamics in methyl bromide with attosecond transient absorption spectroscopy. *Nature Communications* **10**, 3133 (2019).

22. Komarova KG, Remacle F, Levine RD. Propagation of nonstationary electronic and nuclear states: attosecond dynamics in LiF. *Mol Phys* **116**, 2524-2532 (2018).

23. Abramovitz M, Stegun I. *A Handbook of Mathematical Functions*. Dover (1972).

24. van den Wildenberg S, Mignolet B, Levine RD, Remacle F. Temporal and spatially resolved imaging of the correlated nuclear-electronic dynamics and of the ionized photoelectron in a coherently electronically highly excited vibrating LiH molecule. *J Chem Phys* **151**, 134310 (2019).

Acknowledgments

This work was supported by the Fonds National de la Recherche Scientifique (Belgium), F.R.S.-FNRS research grants #T.0132.16 and #J.0012.18 and the AMOS program within the Chemical Sciences, Geosciences and Biosciences Division of the Office of Basic Energy Sciences, Office of Science, US Department of Energy, Award #DE-SC0012628. Computational resources have been provided by the Consortium des Equipements de Calcul Intensif (CECI), funded by the F.R.S.-FNRS under Grant # 2.5020.11. Support of the COST action Attochem(CA18222) is also acknowledged. We thank Prof. Wen Li for useful discussions on the experimental aspects, Dr. Stephan van den Wildenberg for the computation of the photoionization matrix elements and Dr. Benoit Mignolet for his careful reading of the manuscript.

Author contributions.

CMG carried out the electronic structure and quantum dynamics computations. FR and RDL designed the research and wrote the paper with inputs from CMG.

Competing interest

The authors declare no conflict of interests.

Supplementary information

Supplementary figures, Tables and movies are available online